


Methods

In vivo quantification of plant starch reserves at micrometer resolution using X-ray microCT imaging and machine learning

J. Mason Earles^{1*} , Thorsten Knipfer^{2*}, Aude Tixier³, Jessica Orozco³, Clarissa Reyes², Maciej A. Zwieniecki³, Craig R. Brodersen¹ and Andrew J. McElrone^{2,4}

¹School of Forestry and Environmental Studies, Yale University, New Haven, CT 06511, USA; ²Department of Viticulture and Enology, University of California, Davis, CA 95616, USA;

³Department of Plant Sciences, University of California Davis, One Shields Ave., Davis, CA 95616, USA; ⁴Crops Pathology and Genetics Research Unit, USDA-ARS, Davis, CA 95618, USA

Summary

Authors for correspondence:

J. Mason Earles

Tel: +1 415 870 0204

Email: j.earles@yale.edu

Andrew J. McElrone

Tel: +1 530 754 9763

Email: ajmcelrone@ucdavis.edu

Received: 1 November 2017

Accepted: 22 January 2018

New Phytologist (2018) **218**: 1260–1269

doi: 10.1111/nph.15068

Key words: machine learning, nonstructural carbohydrates, ray and axial parenchyma, starch, X-ray microCT.

• Starch is the primary energy storage molecule used by most terrestrial plants to fuel respiration and growth during periods of limited to no photosynthesis, and its depletion can drive plant mortality. Destructive techniques at coarse spatial scales exist to quantify starch, but these techniques face methodological challenges that can lead to uncertainty about the lability of tissue-specific starch pools and their role in plant survival.

• Here, we demonstrate how X-ray microcomputed tomography (microCT) and a machine learning algorithm can be coupled to quantify plant starch content *in vivo*, repeatedly and nondestructively over time in grapevine stems (*Vitis* spp.).

• Starch content estimated for xylem axial and ray parenchyma cells from microCT images was correlated strongly with enzymatically measured bulk-tissue starch concentration on the same stems. After validating our machine learning algorithm, we then characterized the spatial distribution of starch concentration in living stems at micrometer resolution, and identified starch depletion in live plants under experimental conditions designed to halt photosynthesis and starch production, initiating the drawdown of stored starch pools.

• Using X-ray microCT technology for *in vivo* starch monitoring should enable novel research directed at resolving the spatial and temporal patterns of starch accumulation and depletion in woody plant species.

Introduction

Immobilization, aggregation and storage of photosynthate as starch provide a buffer mechanism that permits plants to maintain cellular processes, growth and defense functions in periods when metabolic demand exceeds energetic supply. Plants adjust starch synthesis and degradation rates in response to various environmental and phenological cues with the associated kinetics varying along hourly to seasonal timescales (Smith & Stitt, 2007; Gibon *et al.*, 2009; Sulpice *et al.*, 2009). Consequently, starch is a central molecule involved in the metabolic regulation of a plant's growth trajectory. Further, during periods of low to no photosynthesis, depletion of stored starch is thought to underlie stress-induced mortality associated with drought and pathogenic infection (McDowell, 2011; Sevanto *et al.*, 2014; Dickman *et al.*, 2015). Despite the importance of starch for plant function, only destructive methods with limited spatial resolution exist for quantifying and monitoring starch storage and depletion. These

technical limitations eliminate the opportunity for repeated measurements, introduce substantial across-sample variability, and limit conclusions to bulk tissue. Furthermore, a recent multi-laboratory experiment testing identical starch samples (Germino, 2015; Quentin *et al.*, 2015) showed that methodological variability leads to highly inconsistent results between research groups, which precludes direct, quantitative comparisons between datasets. Problems related to quantification of starch also arise from the spatial and temporal dynamics of the storage and subsequent utilization of starch by the plant. To obtain a more comprehensive understanding of the role of this transient compound, it is necessary to develop tools that can capture the spatiotemporal dynamics of processes related to carbohydrate accumulation and depletion in the intact plant (Bansal & Germino, 2009; Adams *et al.*, 2013; Rosas *et al.*, 2013; Richardson *et al.*, 2015).

Recently, X-ray microcomputed tomography (microCT) has emerged as a nondestructive technique that can be used to create digital cross-sections of a physical object, such as plant tissue, with micrometer- and submicrometer-scale resolution. The absorption of X-rays as a function of an object's physical and

*These authors contributed equally to this work.

chemical properties makes possible spatial segmentation by material type in biological organisms. In plants, X-ray microCT has primarily been used to segment air, water and cell wall domains, which have low to high X-ray absorption coefficients, respectively (Steppe *et al.*, 2004; Brodersen *et al.*, 2011; Herremans *et al.*, 2013; Th  roux-Rancourt *et al.*, 2017). As a result, previous studies employed X-ray microCT to quantify the transition between water- and air-filled vascular conduits in plant stems and leaves (Brodersen *et al.*, 2013; Knipfer *et al.*, 2015a), along with three-dimensional segmentation of anatomical features in fruits, seeds, leaves, and roots (Dhondt *et al.*, 2010; Knipfer *et al.*, 2015b; Cuneo *et al.*, 2016; Th  roux-Rancourt *et al.*, 2017). The chemical and structural similarities between starch and cell wall material, especially cellulose, suggest that these molecules may similarly absorb X-ray energy. Unlike cell wall material, however, starch is a transient molecule that occupies cellular regions otherwise filled with a less dense cytosolic liquid. Hence, we hypothesize that differences in X-ray absorption within the cell interior correspond with the volumetric predominance of starch granules vs cytosolic liquid.

To quantify starch concentrations *in vivo* it is necessary to identify the sites of starch storage and characterize the cells where starch accumulates. Cells containing starch exist throughout most plant organs, including leaves, stems and roots. Ray and axial parenchyma (RAP), and in some species fibers with living protoplasts, serve as the primary sites for long-term starch storage in woody stems (Fahn & Leshem, 1963; Plavcov   *et al.*, 2016). Across a diverse range of temperate tree species possessing a variety of RAP cell shapes and sizes, the cellular fraction comprising RAP tissue has been linked to increased concentration of nonstructural carbohydrates (Plavcov   *et al.*, 2016; Pratt & Jacobsen, 2016). Thus, RAP cells represent the primary site for starch storage and thus a promising target for X-ray microCT analysis of starch content. RAP cells are surrounded by a secondary cell wall and are easily distinguishable in microCT images from nonliving and lignified tissue found in the xylem, such as fibers and vessels (Steppe *et al.*, 2004; Bulcke *et al.*, 2009; Brodersen, 2013). At the same time, substantial variability exists with respect to RAP cell shape and dimension, even within an individual plant (Morris *et al.*, 2016). Consequently, detection of starch using microCT imaging in RAP tissue will require more sophisticated computational techniques beyond simple statistical descriptors, such as the local mean and variance of X-ray absorption, to differentiate starch from the surrounding cellular components.

Here, we quantify and monitor starch *in vivo* at micrometer-scale resolution in stem RAP tissue in the model plant system of grapevine (*Vitis* spp.) using X-ray microCT and a supervised machine learning algorithm. Not only is grapevine a commercially important agricultural woody species, its genome is fully sequenced and its RAP tissue is similar to many other woody species. We apply this technique to spatially map *in vivo* regions of starch depletion in plants experiencing prolonged darkness. Such *in vivo* starch analysis at micrometer resolution should enable novel research directions across the plant sciences.

Materials and Methods

Plant specimen

Grapevine plants (*Vitis riparia*, *V. champinii*, *V. berlandieri*) were grown from 5- to 10-cm-long herbaceous cuttings obtained from established parent plants at the University of California, Davis's experimental vineyards (Knipfer *et al.*, 2015a,b). Cuttings were transplanted into 0.7–1 l plastic pots filled with a soil mix of 40% washed sand, 20% sphagnum peat moss, 20% redwood compost, and 20% pumice rock. Subsequently, plant growth was maintained for 4–12 wk under glasshouse conditions (approximate day : night temperature of 25 : 8  C, light : dark photoperiod of 15 : 9 h, relative humidity of 35%, and photosynthetic active radiation of 500 $\mu\text{mol m}^{-2} \text{s}^{-1}$ during the day). In the glasshouse, plants were drip-irrigated twice daily with water supplemented with calcium (90 $\mu\text{g ml}^{-1}$), magnesium (24 $\mu\text{g ml}^{-1}$), potassium (124 $\mu\text{g ml}^{-1}$), nitrogen as NH_4^+ (6 $\mu\text{g ml}^{-1}$), nitrogen as NO_3^- (96 $\mu\text{g ml}^{-1}$), phosphorus (26 $\mu\text{g ml}^{-1}$), sulfur (16 $\mu\text{g ml}^{-1}$), iron (1.6 $\mu\text{g ml}^{-1}$), manganese (0.27 $\mu\text{g ml}^{-1}$), copper (0.16 $\mu\text{g ml}^{-1}$), zinc (0.12 $\mu\text{g ml}^{-1}$), boron (0.26 $\mu\text{g ml}^{-1}$), and molybdenum (0.016 $\mu\text{g ml}^{-1}$) at pH 5.5–6.0. Plants were maintained under well-watered conditions until analysis (*c.* 0.3 m tall with *c.* 0.01 m diameter stems). MicroCT imaging and corresponding enzymatic validation were performed on a total of *n* = 12 well-watered plants. An additional set of *n* = 6 well-watered plants were selected for testing the effect of dark treatment on starch composition in RAP tissue. Thirty days before microCT scanning, three randomly selected plants were placed in a cardboard box to eliminate light availability, that is, 'deep shade' treatment. The other three plants continued to be grown at *c.* 200 $\mu\text{mol m}^{-2} \text{s}^{-1}$ photosynthetic photon flux density (PPFD).

X-ray microCT imaging

Plants were scanned at the microCT facility (Beamline 8.3.2) at the Lawrence Berkley National Laboratory Advanced Light Source (ALS) (for details, see Brodersen *et al.*, 2010; McElrone *et al.*, 2013; Knipfer *et al.*, 2015a,b). On the day of scanning, plants were transported from the glasshouse to the ALS around 3 h before the start of analysis. For visualization of plant tissue, the pot of an intact plant was placed in an aluminum cage and fixed on an air-bearing stage. To reduce vibrations and stem movement during the scan, a plastic cylinder was mounted on top of the aluminum cage. After the plant was set up properly, a 1–5 mm section of the stem just above the soil was scanned in the 19–21 keV synchrotron X-ray beam using the continuous tomography setting that yields 1025 two-dimensional images with a 3.2- μm -pixel resolution captured on a CMOS camera (PCO.edge; PCO AG, Kehlheim, Germany). The acquired two-dimensional projection images were reconstructed into a stack of transverse images with a custom software plugin for Fiji imaging-processing software (www.fiji.sc, IMAGEJ) that used OCTOPUS 8.3 software (Institute for Nuclear Sciences) in the background. The scanned stem portion was harvested and stored at –20  C prior

to enzymatic starch analysis. The three-dimensional images of plant tissue were generated using AVIZO 6.2 software (VSG).

RAP starch content classification using X-ray microCT and machine learning

The RAP fraction full of starch was classified using a supervised Random Forest machine learning algorithm. For each stem segment, the central slice of the full microCT image stack was selected. Raw microCT images were opened in IMAGEJ (Schindelin *et al.*, 2012) and each RAP boundary was visually outlined and defined as a 'region of interest' (ROI), resulting in *c.* 30 individual RAPs per stem segment. Next, 10 RAP polygons per stem sample were randomly selected for training the Random Forest classification algorithm. Training was done by visually identifying regions in which the RAP cell lumen was present (i.e. empty of starch) or absent (i.e. full of starch). These ROI polygon files were then saved in '.zip' format from the IMAGEJ ROI manager for subsequent import into PYTHON (Python Software Foundation). After this, 10 RAP ROI polygons were selected to be labeled as full/empty of starch.

The microCT images of the 12 stem samples were divided into training and test datasets. This is necessary to test model performance on data that were not used for training and to avoid overfitting to the training dataset. We split the data into training and test groups by visually categorizing the plants into empty, partly full, and mostly full RAP groups which resulted in four plants per category. Then, we assigned two plants from each category to either a training or testing dataset. The raw microCT images selected for each dataset can be downloaded from the associated Github repository (<https://github.com/masonearles/PlantStarchCT>).

Several preprocessing steps were needed to successfully train a classifier that could generalize across the wide range of anatomical variability observed in our dataset. First, to remove local outliers, microCT images were denoised using total variation denoising, that is, the ROF denoise function (Rudin *et al.*, 1992) in IMAGEJ. This was done to remove distinct differences in the variance of nonstem air pixels. As these pixels should theoretically have the same variance of X-ray absorption, we assume such differences are a result of measurement noise. To remove this undesirable source of variance, we chose the ROF denoising parameter in IMAGEJ, that is, sigma, such that the new variance of these nonstem air pixel regions were $\pm 10\%$ across all samples. These denoised images were then saved and opened, along with all ROIs, in PYTHON. Using the RAP ROI polygons, areas outside the RAPs were masked (i.e. set to 'NaN'). The microCT images were then labeled as empty vs full of starch by setting the values equal to '0' and '1', respectively. To remove nonplant background data and improve computational efficiency, rectangular polygon ROIs that define the plant stem boundaries were generated in IMAGEJ for each sample, imported into PYTHON, and used for cropping. Using contrast stretching, we then centered and scaled each image histogram to be bound within the lower 1.5th and 98.5th percentiles of the pixel intensity values contained within each plant's RAP regions.

Various types of feature layers were generated by convolving the preprocessed images with various types of kernels (e.g. Gaussian, variance, lines, and patches) in an attempt to capture the spatial patterns in X-ray absorption of starch, parenchymal cells, and cell wall tissue. In the final model we used four basic types of feature layers. First, we used the preprocessed microCT image. Second, we used three Gaussian filters with SD values of 1, 3 and 5, and kernel dimensions of 3, 9 and 15 pixels, respectively. This filter blurs the image based on neighboring pixel values, with the relative weight decreasing with distance and defined by the SD parameter. Third, we used the sum, minimum, maximum and mean of five variance filters with kernel dimensions of 5, 7, 15, 21 and 29 pixels. This filter was selected to capture the higher degree of variance observed in empty starch regions that resulted from the presence of bright cell wall boundaries and dark cell interiors, as opposed to the lower variance resulting from a relatively homogenous appearance of the RAP tissue when starch was presumed to be present. By combining variance filters of different sizes, we aimed to account for the wide range of RAP cell dimensions observed. Fourth, we applied the three Gaussian filters described earlier to the mean of the variance filters also described earlier. Membrane projection filters and patch filters were also tested, but did not improve model classification (see associated code in Github repository). Overall, we ended up with 11 feature layers that were used to predict empty vs full RAP pixels.

A Random Forest algorithm from the PYTHON Scikit-Learn library (Pedregosa *et al.*, 2011) was used to train a classification model that predicted empty vs full RAP pixels based on the 11 feature layers. To avoid biasing the model toward plants with a greater amount of RAP tissue, and thus proportionally more pixels, we expanded the dataset such that an equal number of pixels were randomly drawn for images from each plant. We trained the Random Forest algorithm on 10 RAP files from the six training data images using 100 decision trees and found that the other default model parameters in the Scikit-Learn Random Forest classification algorithm produced the best results. This model was then used to make predictions on 10 RAP files from the six test data images, and ultimately for the remaining unlabeled RAP regions across all stem segments. Out-of-bag prediction accuracy was used to determine model performance within the training dataset. We generated a confusion matrix using the test data and calculated five performance metrics (see later Fig. 5): accuracy (ACC), detection precision of empty/full regions ($P_{\text{empty}}/P_{\text{full}}$), and detection sensitivity of empty/full regions ($S_{\text{empty}}/S_{\text{full}}$). ACC is the probability of positively or negatively classifying a RAP pixel as either full/empty. Detection precision is the probability that the algorithm correctly predicts if a RAP pixel is full/empty. Detection sensitivity is the probability of detecting the presence of a full/empty RAP pixel.

Using this technique permitted the comparison of RAP fraction classified as full of starch with enzymatically measured starch. Further, we were able to spatially map starch distribution within stem segments at the micrometer scale. Linear models were used to test for the strength of the relationship between RAP fraction classified as full of starch and enzymatically measured starch values.

Enzymatic nonstructural carbohydrate measurement

We measured soluble carbohydrates in woody stem tissue following removal of the bark and presumably phloem using a fresh razor blade (Leyva *et al.*, 2008). In short, 1 ml of deionized water was added to 50 mg of dried tissue, vortexed, heated to 72°C for 15 min, and spun at 21 000 *g* for 10 min. A 50 µl aliquot of the supernatant was diluted ($\times 25$) and mixed with 150 µl of sulfuric acid (98%) and anthrone (0.1%, w/v) solution in a 96-well microplate. The precipitated pellet was reserved for later starch analysis. The plate was cooled on ice at *c.* 4°C for 10 min, then heated to 100°C for 20 min, and finally left to adjust to room temperature for 20 min (22°C). We determined the sugar concentrations as glucose equivalents from the colorimetric reading (Thermo Scientific Multiskan, Waltham, MA, USA) of absorbance at 620 nm (A_{620}) using a predetermined standard curve (0, 0.01, 0.03, 0.1 and 0.3 mg l⁻¹ glucose), and multiplied the result by a measured average wood density of 0.63 g cm⁻³. After extracting the soluble carbohydrates as described earlier, the remaining pellet was processed further to determine tissue concentrations of starch. After two washes with 80% ethanol, the pellet was exposed to 100°C for 10 min and submitted to enzymatic digestion for 4 h in an acetate buffer (pH = 5.5) with 0.7 U of amylase and 7 U of amyloglucosidase at 37°C. Once the digestion was finished, samples were centrifuged for 5 min at 21 000 *g* and the supernatant was diluted 1 : 20 and quantified using the method described earlier.

Results and discussion

Visualization of RAP tissue using X-ray microCT

Ray and axial parenchyma tissue domains were clearly identifiable in grapevine stems based on cell size and orientation when examined using X-ray microCT (Fig. 1). Rays extended from the outer pith perimeter, through the xylem and phloem, and ended at the cortex. In the example shown in Fig. 1, both transverse and longitudinal sections through the RAP tissue revealed two distinct regions (Fig. 1c,d). RAP tissue near the cortex had clearly visible rectangular parenchyma cells that exhibited a strong contrast between the cell wall and lumen (termed 'empty' and highlighted with a yellow polygon in Fig. 1c). RAP cell walls had relatively high X-ray absorption, whereas X-ray absorption in the cell interior was more like that seen in water-filled vessel interiors (Fig. 2). Conversely, RAP tissue more proximal to the pith had a granular texture in which the cell wall and lumen were not visible (termed 'full' and highlighted with a magenta polygon in Fig. 1c). These RAP regions generally had higher overall X-ray absorption, similar to that in cell wall material (Fig. 2). Further, they contained small bright spots that superficially resemble starch granules in both size and shape, which is granular in its crystalline form as previously observed in optical sections stained with potassium iodide (e.g. Czemmell *et al.*, 2015). The observation of lower and higher X-ray-absorbing regions within RAP tissue corroborated

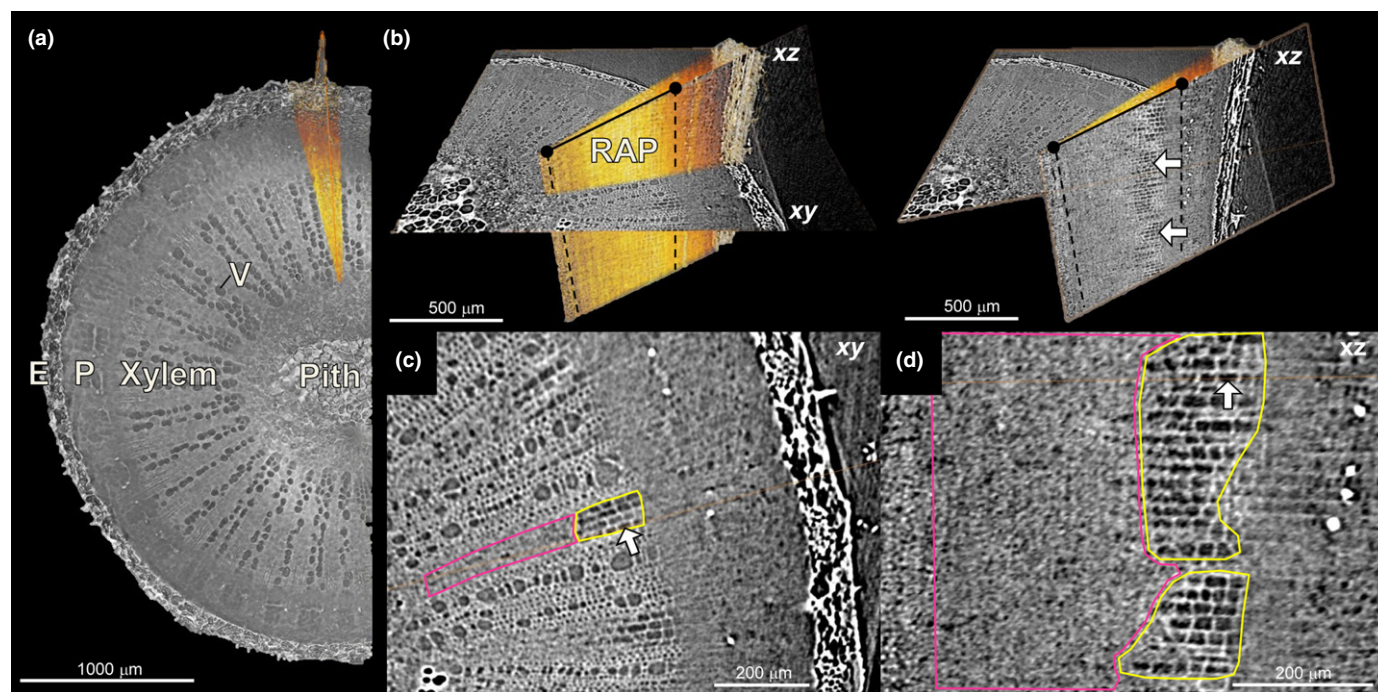


Fig. 1 Visualization of grapevine stem tissue using X-ray microcomputed tomography. (a) Volume rendering showing a transverse section through the stem (E, epidermis; P, phloem; V, vessel). Ray and axial parenchyma (RAP) are located in xylem tissue between radial files of vessels (highlighted in yellow/orange color). (b) Three-dimensional representation of RAP (enclosed by dashed line) embedded in stem xylem tissue (left-hand panel), and corresponding longitudinal image slice through RAP (enclosed by dashed line) showing parenchyma cells devoid of solid, putative starch granules in dark gray color (examples indicated by arrows) (right-hand panel). Transverse and longitudinal images sectioning through the RAP are indicated as xy- and xz-slices, respectively. (c, d) Enlarged transverse (c) and longitudinal (d) images corresponding to (b) visualizing the composition of RAP tissue. Two RAP regions can be visually distinguished by their shape and texture: full (magenta polygons) or empty (yellow polygons).

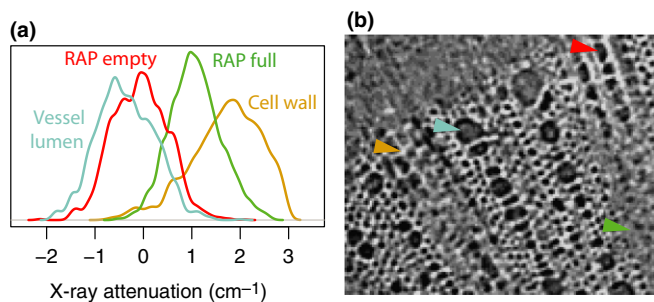


Fig. 2 (a) Probability density plots showing the linear X-ray attenuation coefficients (absorption cm^{-1}) of vessel lumen (blue), ray and axial parenchyma (RAP) empty (red), RAP full (green), and cell wall (gold) in *Vitis* sp. with examples of corresponding regions shown in (b). Negative values result from the log transformation of X-ray transmission required to calculate absorption.

our initial hypothesis that such differences should exist in correspondence with the distinct molecular structure of water, starch and cell wall material. However, it should be noted that other cytosolic compounds solid in nature may interfere with our detection methods, but to date we are not aware of such phenomenon.

RAP tissue classification as full or empty via supervised machine learning

To test if regions of cells that visually appeared full/empty corresponded with the presence/absence of starch required a technique for quantifying the distinct X-ray absorption patterns visible in the microCT images. Trainable machine learning algorithms have emerged in recent years as a powerful computational technique for detecting complex visual patterns. Initially, the user defines a set of distinct classes and the computer refines an algorithm that minimizes the classification error based on a set of

image filters utilized for visual feature detection. Given the substantial amount of morphological variability in RAPs (Plavcová *et al.*, 2016), such a technique was especially relevant. Classifying 10 RAP regions in six stems as either full or empty types (Figs 3, 4) resulted in a prediction accuracy of $74 \pm 3\%$ (1 SE; Fig. 5) for the test dataset ($n=6$) and $97 \pm 1\%$ (Fig. 5) for the training dataset ($n=6$). Moreover, the model had relatively high sensitivity and precision for full and empty regions (Fig. 5). After training the classifier, we applied it to the remaining 20–30 unlabeled RAP regions for each stem sample (Fig. 3c). Across the 12 stem samples, this resulted in predictions that full-type features occupied 16–73% of RAP tissue (Fig. 6). From Fig. 6 it is clear that the fraction of full-type features was independent of stem diameter. Preprocessing, training on *c.* 1.5 million pixels, and predicting a similar number of pixels took *c.* 5 CPU min on a quad-core machine.

Our initial efforts attempted to use simple statistical descriptors of the RAP regions, such as the mean, variance, and kurtosis of the X-ray absorption values. However, a high degree of within- and among-sample variability precluded the use of such techniques. For example, in empty regions RAP cell lumen size ranged from < 6 to $> 81 \mu\text{m}^2$. This caused substantial variability in the proportion of cell wall to lumen present in RAPs, resulting in a broad set of mean and variance values within and across samples. Other sources of variability with respect to X-ray absorption were also present as a result of, for instance, energy fluctuation of the X-ray beam, diffraction patterning, and X-ray absorption edge effects.

Predicting enzymatically measured starch content at micrometer-scale resolution

Enzymatically measured starch concentration for the classified samples ranged from 3 to 84 mg g^{-1} (Fig. 6). Visual inspection

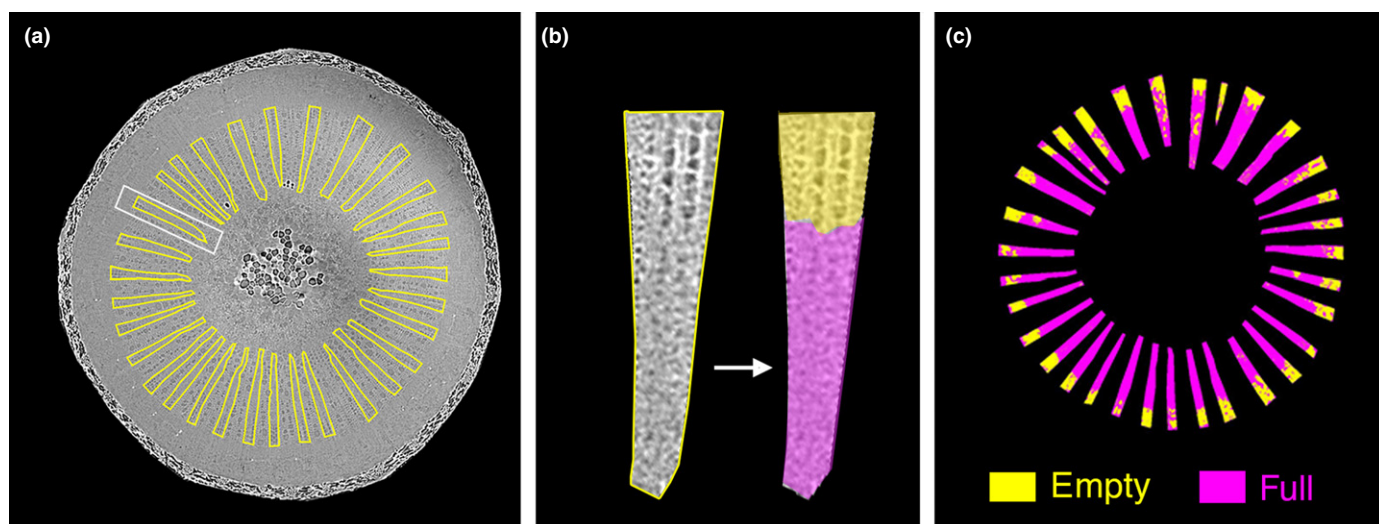


Fig. 3 Illustration of Random Forest machine learning segmentation of full (magenta) and empty (yellow) ray and axial parenchyma (RAP) regions from microcomputed tomography images. The technique consisted of: (a) manually defining RAP regions in the cross-section of grapevine stems; (b) manually classifying pixels as visually appearing full (magenta polygons) or empty (yellow polygons) for 10 RAP regions in six training images for the Random Forest machine learning algorithm; and (c) automatically classifying pixels as full or empty based on the initial training data for the test images and the remaining 20–30 RAP regions in the training images.

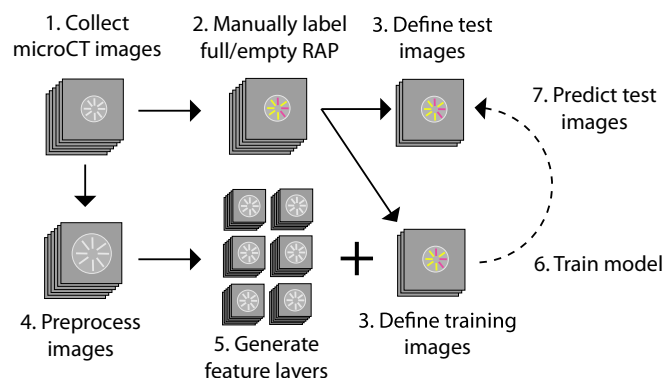


Fig. 4 Machine learning framework for *in vivo* quantification of starch in plant stems (*Vitis* sp. shown). (1) X-ray microcomputed tomography (microCT) images of the stem cross-section were collected as 32-bit images. (2) Visually empty/full parenchymal regions were manually labeled as full or empty of starch. (3) Manually labeled images were split equally into test and training image datasets. (4) MicroCT images were preprocessed (i.e. cropped, denoised, and contrast stretched) to normalize images across plant samples and to facilitate learning by the training algorithm. (5) Feature layers were generated by convolving the preprocessed images with various types of kernels (e.g. Gaussian, variance, lines, and patches) that corresponded with spatial patterns in X-ray absorption of starch, parenchymal cells, and cell wall tissue. (6) A Random Forest algorithm was used to train a model to predict the labeled training images based on available feature layers. (7) The trained model was used to predict empty/full ray and axial parenchyma (RAP) regions in test images that were not used for training and the model's performance was evaluated.

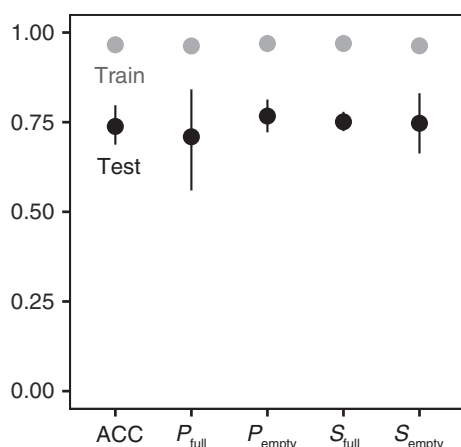


Fig. 5 Performance metrics for segmentation of the training ($n=6$; gray points and lines) and test ($n=6$; black points and lines) images using the Random Forest machine learning algorithm of *Vitis* sp., assuming manual segmentation for 10 ray and axial parenchyma (RAP) files per sample as 'groundtruth' values. ACC, accuracy; P_{full} , precision for predicting full RAP regions; P_{empty} , precision for predicting empty RAP regions; S_{full} , sensitivity for predicting full RAP regions; S_{empty} , sensitivity for predicting empty RAP regions. Mean value of each performance metric for all six samples and 1 SE are shown. Note that all metrics are fractional and, therefore, range from 0 to 1.

revealed that samples in which full regions comprised a large fraction of RAP tissue also tended to have high starch concentrations as measured enzymatically. On the other hand, samples

in which RAP tissue comprised predominantly empty regions had low enzymatically measured starch concentrations. At the entire stem level we found a strong positive relationship between the RAP fraction classified as full via machine learning and the starch content measured destructively using enzymatic digestion (Fig. 7; linear fit, $R^2=0.94$, $P<0.001$). This finding provides support for our initial hypothesis that differences in the spatial patterns of X-ray absorption in RAP tissue should correspond with the volumetric predominance of starch granules vs cytosolic liquid.

Light is essential for photosynthetic production, and in turn the absence of light forces a plant to deplete its starch reserves (Chang, 1980). We tested the ability of X-ray microCT to capture this predicted decline in starch within plants that were maintained for 30 d in darkness (i.e. dark treatment) vs a moderate light environment at $c. 200 \mu\text{mol m}^{-2} \text{s}^{-1}$ PPFD (i.e. control). After 30 d, the cell lumens of dark-treated plants were completely devoid of starch granules throughout the entire RAP region (Fig. 8). By contrast, RAP regions of control plants were between 40% and 75% full. By first applying our machine learning algorithm and then using the calibration curve shown in Fig. 7, we estimated that dark-treated plants had starch concentrations of 0 mg g^{-1} , whereas control plants were estimated to have between 52 and 75 mg g^{-1} . Hence, our *in vivo* technique for starch quantification was able to spatially detect and quantify differences in starch depletion as a result of dark treatment.

These observations highlight how the capacity to spatially track starch mobilization within the tissue can provide novel insights beyond classical starch quantification methods. In both experiments, starch depletion did not show an anisotropic spatial pattern, as empty and full cells were adjacently located, forming relatively full or empty domains. These patterns could have implications for carbohydrate management at the whole-plant level. The absence and mobilization of starch seemed to begin at the wood periphery and progressed in a centripetal direction toward the stem center (Figs 6, 8). Previous research showing low variation of starch concentrations at the center of tree trunks suggested that these pools act as buffers at multi-annual scales (Hartmann & Trumbore, 2016). Such an anatomical pattern would presumably only allow starch accumulation in outer RAP cells once inner RAP cells were already filled with starch. On the other hand, emptying of starch-filled cells seemed to occur from the outermost RAP cells toward the phloem. Such a pattern could be the result of a low soluble sugar concentration in the apoplast (Carpaneto *et al.*, 2005, 2010; Secchi & Zwieniecki, 2016) owing to a diffusional gradient maintained by a leaky phloem (Knoblauch & van Bel, 1998). Thus, the proximity of the phloem and cambium to peripheral starch depletion in wood might provide an explanation for this mobilization pattern, ensuring fast and efficient radial transport to the outermost RAP tissues requiring carbohydrates for respiration (Tyree *et al.*, 1999).

X-ray microCT images indicated that RAP cells tend to be either full or empty with a relatively sharp border between RAP domains categorized as empty and full. This feature made the machine learning a relatively straightforward process, and could

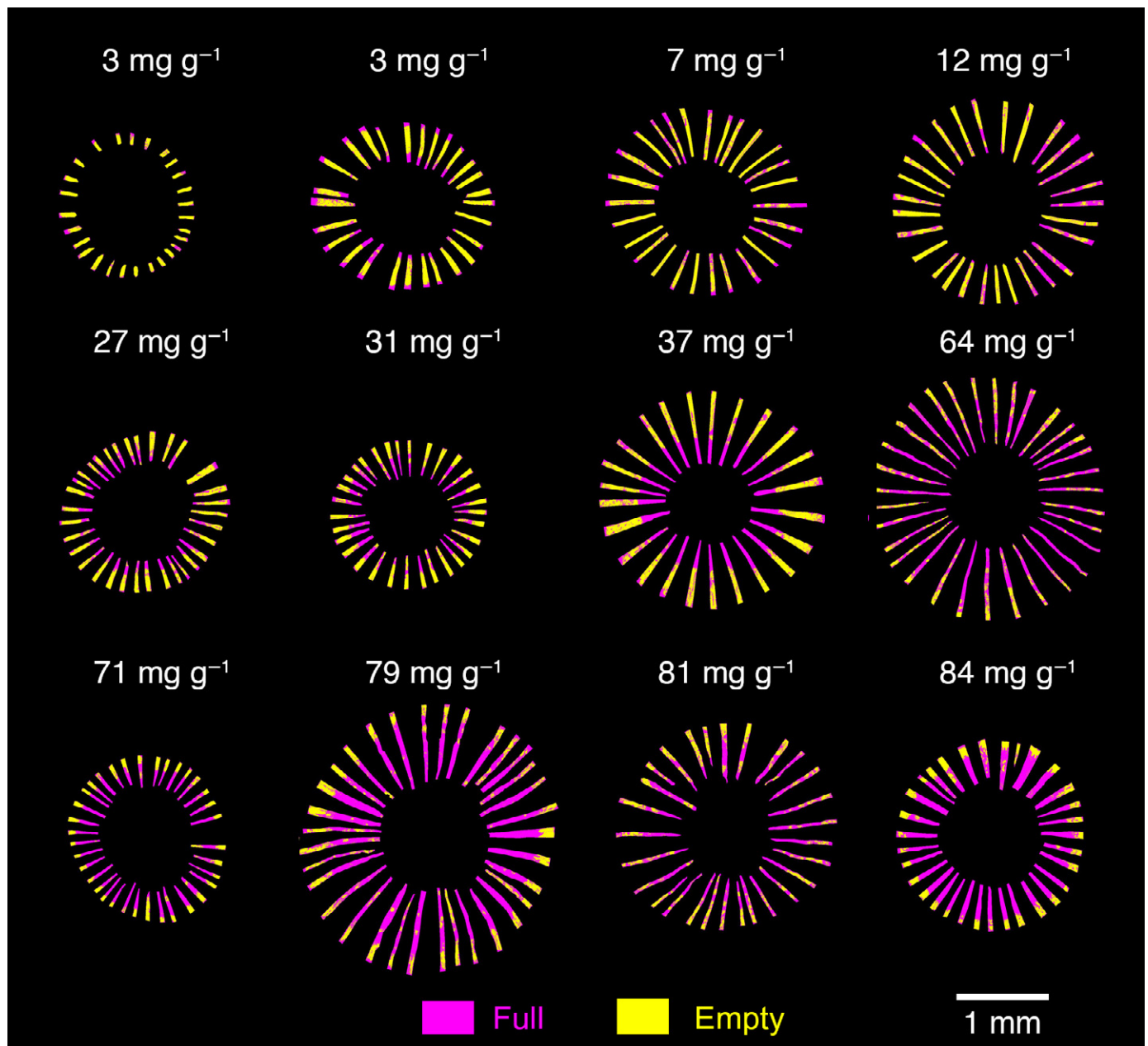


Fig. 6 Spatial maps of regions predicted as full (magenta) or empty (yellow) in ray and axial parenchyma (RAP) tissue of 12 *Vitis* spp. stems. The corresponding enzymatically measured starch concentration for each plant is provided above the RAP map.

have important implications for our biological understanding of starch reserve formation and utilization, particularly in model systems such as *Vitis vinifera* or *Arabidopsis thaliana*, where the linkages between gene expression and starch metabolism are better understood (Dai *et al.*, 2013; Feike *et al.*, 2016; Zhu *et al.*, 2017). Local changes in carbohydrate availability could trigger whole-cell responses in enzymatic activity toward either continuous accumulation or degradation, but less commonly toward an intermediate status of being partly full. This relatively binary pattern seemed to be spatially constrained, as empty and full cells seemed to be adjacent to each other, forming contiguous full or empty domains.

Using X-ray microCT for *in vivo* starch quantification presents various limitations and opportunities for refinement. X-ray microCT instruments are not available at many institutions and require expert knowledge to operate. Further, there is typically a tradeoff between field-of-view and feature resolution, which potentially limits the size of samples that can be scanned. For example, we suspect that this study was conducted near the minimum feature resolution required for starch detection in grapevine, i.e. *c.* 10 μm (pixel size of 3.2 μm), which corresponded with an 8.8 mm field of view. Thus, if the stem were greater than 8.8 mm in diameter then it would not be entirely visible. At higher magnification/resolution, we observed a finer

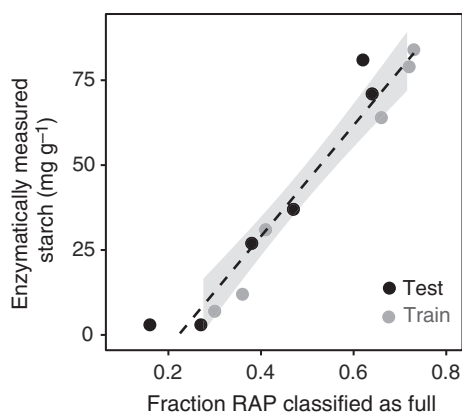


Fig. 7 Relationship between ray and axial parenchyma (RAP) fraction classified as full and empty vs starch content measured destructively using enzymatic digestion in stems of *Vitis* spp. (linear fit, $R^2 = 0.94$, $P < 0.001$; gray polygon is the 95th confidence interval). Each symbol represents the analysis of an individual plant.

detail of starch granules but the field of view becomes progressively smaller. This limitation is, however, instrument-specific. The time required for an individual scan also varies dramatically depending on the instrument. Modern synchrotron radiation sources allow for quick scans in < 5 min, whereas benchtop X-ray microCT scanners can take hours. Further, the damaging effects of X-ray radiation on long-term metabolic activity of plant tissue are not well studied, but we have observed variable responses that depends on tissue type, species, and exposure time. These effects

should be considered, especially when repeatedly scanning plant tissue. Regarding the machine learning technique presented here, the model can be generalized to other plant species but retraining would probably be required.

Conclusion

Here, we demonstrate the ability of X-ray microCT to detect and quantify starch in living plants. Until now, starch could only be measured using destructive techniques. Our novel method presents the opportunity to study carbohydrate metabolism that will permit repeated measurements and lower across-sample variability, all at micrometer-scale spatial resolution. Such studies on carbohydrate metabolism can be coupled with hydraulic studies to improve our understanding of how plants coordinate these two key systems underlying basic plant function, and help to resolve current debates regarding the relative contribution of carbon starvation and hydraulic failure to drought-induced tree mortality (McDowell *et al.*, 2008; Adams *et al.*, 2017; Schwalm *et al.*, 2017). Further, as X-ray microCT is becoming increasingly common across the plant sciences, a large amount of data is amassing, and our technique can be applied retroactively to existing datasets to analyze the spatial distribution of starch depletion, with simple modifications to the algorithm to account for variability in starch morphology and chemistry across species. We expect that *in vivo* starch detection should be applicable to many other plant species found in both agricultural and natural systems, providing high spatiotemporal detail for investigating how carbohydrate

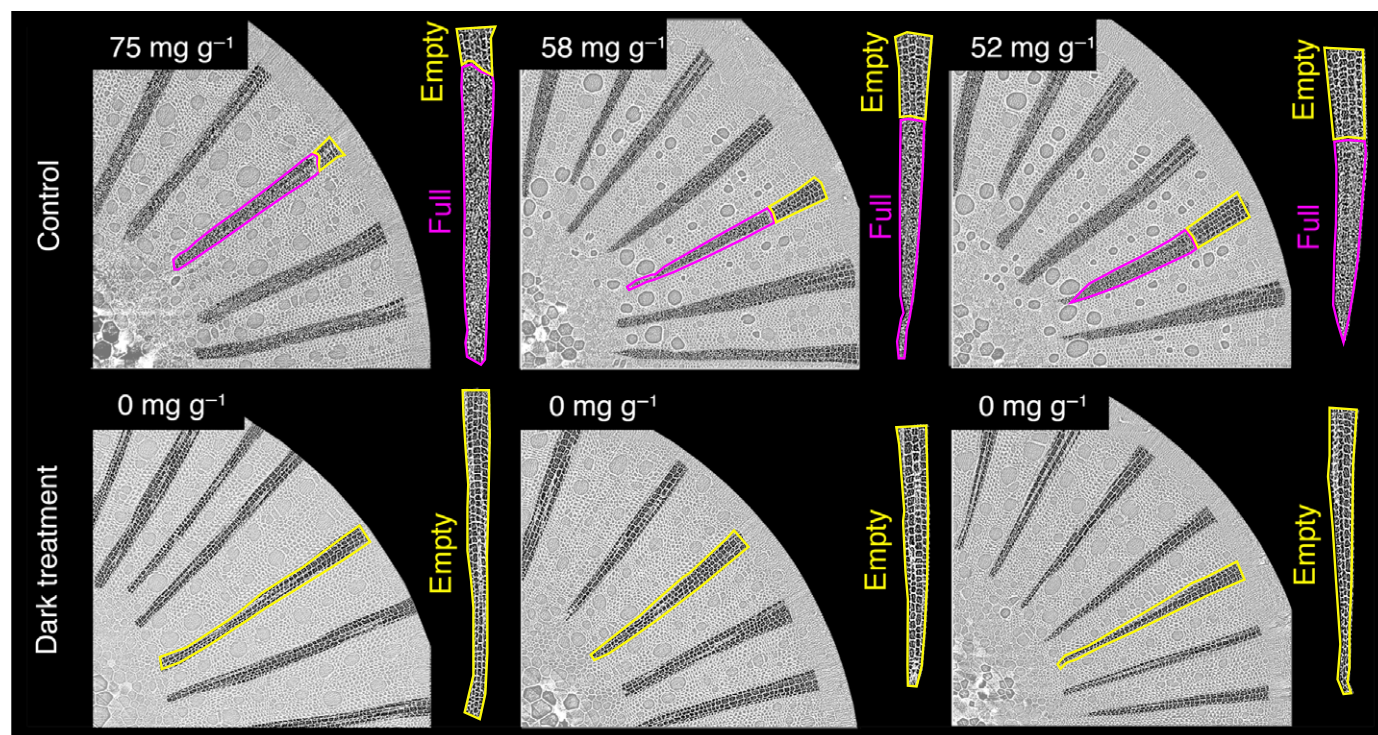


Fig. 8 Control ($n = 3$; top row) vs dark-treated ($n = 3$; bottom row) stem cross-sections from six *Vitis champini* plants. Visually full (magenta) vs empty (yellow) regions are outlined. Estimated starch values using machine learning algorithm are provided in the upper left corner of each image. Image contrast in regions outside of ray and axial parenchymas (RAPs) was lightened to highlight RAP cellular regions.

metabolism responds to key stresses such as shade, drought, freezing, salinity, and pathogenic infection. The capacity for *in vivo* observation of starch content in stems opens the door for new experimental work aimed at directly and locally manipulating the stem internal environment, providing time-resolved quantification of plant nonstructural carbohydrate utilization.

Author contributions

J.M.E. conceived the study, developed the computational approach, performed the experiments, analyzed the data, and wrote the manuscript. T.K. conceived the study, performed the experiments, and revised the manuscript. A.T. performed some of the experiments and revised the manuscript. J.O. performed some of the experiments. C.R. performed some of the experiments and analyzed the data. M.A.Z. revised the manuscript. C.R.B. revised the manuscript. A.J.M. conceived the study and revised the manuscript.

ORCID

J. Mason Earles  <http://orcid.org/0000-0002-8345-9671>

References

- Adams HD, Germino MJ, Breshears DD, Barron-Gafford GA, Guardiola-Claramonte M, Zou CB, Huxman TE. 2013. Nonstructural leaf carbohydrate dynamics of *Pinus edulis* during drought-induced tree mortality reveal role for carbon metabolism in mortality mechanism. *New Phytologist* 197: 1142–1151.
- Adams HD, Zeppel MJB, Anderegg WRL, Hartmann H, Landhäusser SM, Tissue DT, Huxman TE, Hudson PJ, Franz TE, Allen CD *et al.* 2017. A multi-species synthesis of physiological mechanisms in drought-induced tree mortality. *Nature Ecology & Evolution* 1: 1285–1291.
- Bansal S, Germino MJ. 2009. Temporal variation of nonstructural carbohydrates in montane conifers: similarities and differences among developmental stages, species and environmental conditions. *Tree Physiology* 29: 559–568.
- Brodersen CR. 2013. Visualizing wood anatomy in three dimensions with high-resolution X-ray micro-tomography (μ CT) – a review. *IAWA Journal* 34: 408–424.
- Brodersen CR, Lee EF, Choat B, Jansen S, Phillips RJ, Shackel KA, McElrone AJ, Matthews MA. 2011. Automated analysis of three-dimensional xylem networks using high-resolution computed tomography. *New Phytologist* 191: 1168–1179.
- Brodersen CR, McElrone AJ, Choat B, Lee EF, Shackel KA, Matthews MA. 2013. In vivo visualizations of drought-induced embolism spread in *Vitis vinifera*. *Plant Physiology* 161: 1820–1829.
- Brodersen CR, McElrone AJ, Choat B, Matthews M, Shackel KA. 2010. The dynamics of embolism repair in xylem: In vivo visualizations using high-resolution computed tomography. *Plant Physiology* 54: 1088–1095.
- Bulcke J, Boone M, Acker J, Stevens M, Hoorebeke L. 2009. X-ray tomography as a tool for detailed anatomical analysis. *Annals of Forest Science* 66: 508.
- Carpaneto A, Geiger D, Bamberg E, Sauer N, Fromm J, Hedrich R. 2005. Phloem-localized, proton-coupled sucrose carrier ZmSUT1 mediates sucrose efflux under the control of the sucrose gradient and the proton motive force. *Journal of Biological Chemistry* 280: 21437–21443.
- Carpaneto A, Koepsell H, Bamberg E, Hedrich R, Geiger D. 2010. Sucrose- and H⁺-dependent charge movements associated with the gating of sucrose transporter ZmSUT1. *PLoS ONE* 5: 1–10.
- Chang CW. 1980. Starch depletion and sugars in developing cotton leaves. *Plant Physiology* 65: 844–847.
- Cuneo I, Knipfer T, Brodersen C, McElrone AJ. 2016. Mechanical failure of fine root cortical cells initiates plant hydraulic decline during drought. *Plant Physiology* 172: 00923.2016.
- Czemmel S, Galarneau ER, Travadon R, McElrone AJ, Cramer GR, Baumgartner K. 2015. Genes expressed in grapevine leaves reveal latent wood infection by the fungal pathogen *Neofusicoccum parvum*. *PLoS ONE* 10: 1–21.
- Dai ZW, Léon C, Feil R, Lunn JE, Delrot S, Gomès E. 2013. Metabolic profiling reveals coordinated switches in primary carbohydrate metabolism in grape berry (*Vitis vinifera* L.), a non-climacteric fleshy fruit. *Journal of Experimental Botany* 64: 1345–1355.
- Dhondt S, Vanhaeren H, Van Loo D, Cnudde V, Inzé D. 2010. Plant structure visualization by high-resolution X-ray computed tomography. *Trends in Plant Science* 15: 419–422.
- Dickman LT, McDowell NG, Sevanto S, Pangle RE, Pockman WT. 2015. Carbohydrate dynamics and mortality in a piñon-juniper woodland under three future precipitation scenarios. *Plant, Cell & Environment* 38: 729–739.
- Fahn A, Leshem B. 1963. Wood fibres with living protoplasts. *New Phytologist* 62: 91–98.
- Feike D, Seung D, Graf A, Bischof S, Ellick T, Coiro M, Soyk S, Eicke S, Mettler-Altmann T, Lu KJ *et al.* 2016. The starch granule-associated protein EARLY STARVATION1 is required for the control of starch degradation in *Arabidopsis thaliana* leaves. *Plant Cell* 28: 1472–1489.
- Germino MJ. 2015. A carbohydrate quandary. *Tree Physiology* 35: 1141–1145.
- Gibon Y, Pyl E-T, Sulpice R, Lunn JE, Höhne M, Günther M, Stitt M. 2009. Adjustment of growth, starch turnover, protein content and central metabolism to a decrease of the carbon supply when *Arabidopsis* is grown in very short photoperiods. *Plant, Cell & Environment* 32: 859–874.
- Hartmann H, Trumbore S. 2016. Understanding the roles of nonstructural carbohydrates in forest trees – from what we can measure to what we want to know. *New Phytologist* 211: 386–403.
- Herremans E, Verboven P, Bongaers E, Estrade P, Verlinden BE, Wevers M, Hertog M, Nicolai BM. 2013. Characterisation of ‘Braeburn’ browning disorder by means of X-ray micro-CT. *Postharvest Biology and Technology* 75: 114–124.
- Knipfer T, Eustis A, Brodersen C, Walker AM, McElrone AJ. 2015a. Grapevine species from varied native habitats exhibit differences in embolism formation/repair associated with leaf gas exchange and root pressure. *Plant, Cell & Environment* 38: 1503–1513.
- Knipfer T, Fei J, Gambetta GA, McElrone AJ, Shackel KA, Matthews MA. 2015b. Water transport properties of the grape pedicel during fruit development: insights into xylem anatomy and function using microtomography. *Plant Physiology* 168: 1590–1602.
- Knoblauch M, van Bel AJEJE. 1998. Sieve tubes in action. *Plant Cell* 10: 35–50.
- Leyva A, Quintana A, Sánchez M, Rodríguez EN, Cremata J, Sánchez JC. 2008. Rapid and sensitive anthrone-sulfuric acid assay in microplate format to quantify carbohydrate in biopharmaceutical products: method development and validation. *Biologicals: Journal of the International Association of Biological Standardization* 36: 134–141.
- McDowell NG. 2011. Mechanisms linking drought, hydraulics, carbon metabolism, and vegetation mortality. *Plant Physiology* 155: 1051–1059.
- McDowell N, Pockman WT, Allen CD, Breshears DD, Cobb N, Kolb T, Plaut J, Sperry J, West A, Williams DG *et al.* 2008. Mechanisms of plant survival and mortality during drought: why do some plants survive while others succumb to drought? *New Phytologist* 178: 719–739.
- McElrone AJ, Choat B, Parkinson DY, MacDowell A, Brodersen CR. 2013. Utilization of high resolutions computed tomography to visualize the three dimensional structure and function of plant vasculature. *Journal of Visualized Experiments* 74: e50162.
- Morris H, Plavcová L, Cvecko P, Fichtler E, Gillingham MAF, Martínez-Cabrera HI, Mcglinn DJ, Wheeler E, Zheng J, Ziemińska K *et al.* 2016. A global analysis of parenchyma tissue fractions in secondary xylem of seed plants. *New Phytologist* 209: 1553–1565.
- Pedregosa F, Varoquaux G, Gramfort A, Michel V, Thirion B, Grisel O, Blondel M, Prettenhofer P, Weiss R, Dubourg V *et al.* 2011. Scikit-learn: machine learning in Python. *Journal of Machine Learning Research* 12: 2825–2830.
- Plavcová L, Hoch G, Morris H, Ghiasi S, Jansen S. 2016. The amount of parenchyma and living fibers affects storage of nonstructural carbohydrates in

- young stems and roots of temperate trees. *American Journal of Botany* 103: 603–612.
- Pratt RB, Jacobsen AL. 2016. Conflicting demands on angiosperm xylem: tradeoffs among storage, transport, and biomechanics. *Plant, Cell & Environment* 40: 1–17.
- Python Software Foundation. *Python language reference, version 2.7*. URL <http://www.python.org>.
- Quentin AG, Pinkard EA, Ryan MG, Tissue DT, Baggett LS, Adams HD, Maillard P, Marchand J, Landhäusser SM, Lacomte A *et al.* 2015. Non-structural carbohydrates in woody plants compared among laboratories. *Tree Physiology* 35: 1146–1165.
- Richardson AD, Carbone MS, Huggett BA, Furze ME, Czimczik CI, Walker JC, Xu X, Schaberg PG, Murakami P. 2015. Distribution and mixing of old and new nonstructural carbon in two temperate trees. *New Phytologist* 206: 590–597.
- Rosas T, Galiano L, Ogaya R, Peñuelas JJ, Martínez-Vilalta J. 2013. Dynamics of non-structural carbohydrates in three Mediterranean woody species following long-term experimental drought. *Frontiers in Plant Science* 4: 1–16.
- Rudin LI, Osher S, Fatemi E. 1992. Nonlinear total variation based noise removal algorithms. *Physica D: Nonlinear Phenomena* 60: 259–268.
- Schindelin J, Arganda-Carreras I, Frise E. 2012. Fiji: an open-source platform for biological-image analysis. *Nature Methods* 9: 676–682.
- Schwalm CR, Anderegg WRL, Michalak AM, Fisher JB, Biondi F, Koch G, Litvak M, Ogle K, Shaw JD, Wolf A *et al.* 2017. Global patterns of drought recovery. *Nature* 548: 202–205.
- Secchi F, Zwieniecki MA. 2016. Accumulation of sugars in the xylem apoplast observed under water stress conditions is controlled by xylem pH. *Plant, Cell & Environment* 39: 2350–2360.
- Sevanto S, McDowell NG, Dickman LT, Pangle R, Pockman WT. 2014. How do trees die? A test of the hydraulic failure and carbon starvation hypotheses. *Plant, Cell & Environment* 37: 153–161.
- Smith AM, Stitt M. 2007. Coordination of carbon supply and plant growth. *Plant, Cell & Environment* 30: 1126–1149.
- Steppe K, Cnudde V, Girard C, Lemeur R, Cnudde JP, Jacobs P. 2004. Use of X-ray computed microtomography for non-invasive determination of wood anatomical characteristics. *Journal of Structural Biology* 148: 11–21.
- Sulpice R, Pyl E, Ishihara H, Trenkamp S, Steinfath M, Witucka-wall H, Von Korff M, Caroline M, Gibon Y, Stitt M. 2009. Starch as a major integrator in the regulation of plant growth. *Proceedings of the National Academy of Sciences, USA* 106: 10348–10353.
- Thérroux-Rancourt G, Earles JM, Gilbert ME, Zwieniecki MA, Boyce CK, McElrone AJ, Brodersen CR. 2017. The bias of a two-dimensional view: comparing two-dimensional and three-dimensional mesophyll surface area estimates using noninvasive imaging. *New Phytologist* 215: 1609–1622.
- Tyree MT, Salleo S, Nardini A, Lo Gullo M, Mosca R. 1999. Refilling of embolized vessels in young stems of laurel. Do we need a new paradigm? *Plant Physiology* 120: 11–22.
- Zhu X, Zhang C, Wu W, Li X, Zhang C, Fang J. 2017. Enzyme activities and gene expression of starch metabolism provide insights into grape berry development. *Horticulture Research* 4: 17018.



About New Phytologist

- *New Phytologist* is an electronic (online-only) journal owned by the New Phytologist Trust, a **not-for-profit organization** dedicated to the promotion of plant science, facilitating projects from symposia to free access for our Tansley reviews and Tansley insights.
- Regular papers, Letters, Research reviews, Rapid reports and both Modelling/Theory and Methods papers are encouraged. We are committed to rapid processing, from online submission through to publication 'as ready' via *Early View* – our average time to decision is <26 days. There are **no page or colour charges** and a PDF version will be provided for each article.
- The journal is available online at Wiley Online Library. Visit **www.newphytologist.com** to search the articles and register for table of contents email alerts.
- If you have any questions, do get in touch with Central Office (np-centraloffice@lancaster.ac.uk) or, if it is more convenient, our USA Office (np-usaoffice@lancaster.ac.uk)
- For submission instructions, subscription and all the latest information visit **www.newphytologist.com**